

Spatial resolution of a hard x-ray CCD detector

John F. Seely,^{1,*} Nino R. Pereira,² Bruce V. Weber,³ Joseph W. Schumer,³
John P. Apruzese,³ Lawrence T. Hudson,⁴ Csilla I. Szabo,⁵
Craig N. Boyer,⁶ and Scott Skirlo⁷

¹Space Science Division, Naval Research Laboratory, Washington, D.C. 20375, USA

²Ecopulse Inc., P.O. Box 528, Springfield, Virginia 22150, USA

³Plasma Physics Division, Naval Research Laboratory, Washington, D.C. 20375, USA

⁴National Institute of Standards and Technology, Gaithersburg, Maryland 20899, USA

⁵Artep Inc., 2922 Excelsior Spring Court, Ellicott City, Maryland 21042, USA

⁶L3 Communications, Washington, D.C. 20375, USA

⁷Massachusetts Institute of Technology, Cambridge, Massachusetts 02139, USA

*Corresponding author: john.seely@nrl.navy.mil

Received 25 May 2010; accepted 30 June 2010;
posted 8 July 2010 (Doc. ID 129015); published 4 August 2010

The spatial resolution of an x-ray CCD detector was determined from the widths of the tungsten x-ray lines in the spectrum formed by a crystal spectrometer in the 58 to 70 keV energy range. The detector had 20 μm pixel, 1700 by 1200 pixel format, and a CsI x-ray conversion scintillator. The spectral lines from a megavolt x-ray generator were focused on the spectrometer's Rowland circle by a curved transmission crystal. The line shapes were Lorentzian with an average width after removal of the natural and instrumental line widths of 95 μm (4.75 pixels). A high spatial frequency background, primarily resulting from scattered gamma rays, was removed from the spectral image by Fourier analysis. The spectral lines, having low spatial frequency in the direction perpendicular to the dispersion, were enhanced by partially removing the Lorentzian line shape and by fitting Lorentzian curves to broad unresolved spectral features. This demonstrates the ability to improve the spectral resolution of hard x-ray spectra that are recorded by a CCD detector with well-characterized intrinsic spatial resolution.

OCIS codes: 040.7480, 340.7440, 040.1520.

1. Introduction

X-ray CCD detectors operating in the low energy range, less than approximately 10 keV, can directly detect the x-ray photons with spatial resolution comparable to the pixel size. At higher energies, the detection efficiency is lower because of the limited depth of the silicon depletion region; in addition, the high-energy photons can cause radiation damage to the lattice. In this case, the x-ray energy is converted to optical photons by a scintillator, and the optical photons are detected by the underlying CCD detector. The high-energy x-ray photons deposit energy in a relatively large scintillator volume, and second-

ary electrons can cause increased spreading of the energy. Thus, the optical photons generated by a single x-ray photon are recorded by several contiguous pixels and with reduced spatial resolution.

Because the spatial resolution achieved by a hard x-ray detector is critically important to spectroscopy and radiography, it is necessary to experimentally characterize the detector's intrinsic spatial resolution independent of instrumental effects, including source broadening. The knowledge of the detector's performance can be used to enhance the spatial resolution by Fourier analysis.

Quantitative techniques for accurately determining the spatial resolution achieved by a detector

operating in the visible wavelength region are well developed. The image of a fine line-pair pattern determines the modulation transfer function (MTF), and the inverse Fourier transform of the MTF is the line spread function (LSF), the image of a narrow linear illumination of the CCD. The image of a sharp opaque edge determines the edge transfer function, and its derivative is also equal to the LSF. The LSF can be directly determined from the image formed by illuminating the detector with a single narrow line, where the width of the line is much less than the detector's intrinsic spatial resolution. Finally, in the case of a CCD detector having resolution comparable to or better than the spatial scale of the illumination pattern, aliasing artifacts can result from the orientation of the illumination pattern to the CCD pixel pattern.

In the hard x-ray region, fine line patterns and sharp edges are typically machined from heavy metals, such as lead and tungsten. The object must be sufficiently thick to be opaque to the hard x-rays, and this can limit the spatial scale of the sharp features. Thick objects can also cause vignetting of nonparallel rays. Alternatively, the x-ray detector can be illuminated by a narrow spectral line formed by a focusing x-ray spectrometer, and the measured line shape is the detector's LSF in the absence of other instrumental effects. These techniques were used to characterize the LSF of two types of photo-stimulable image plate detectors in the hard x-ray region [1]. In this paper, we report the measurement of the spatial resolution of a hard x-ray CCD detector illuminated by narrow tungsten spectral lines in the 58 to 70 keV energy range.

2. X-ray Spectrometer and CCD Detector

The experimental setup of the x-ray spectrometer and CCD detector is shown in Fig. 1. The spectrometer is of a type originally developed by Cauchois and more recently adapted for the measurement of the peak kilovoltage of medical radiography x-ray sources [2]. A cylindrically curved crystal, operating in transmission, focuses monoenergetic rays from an extended x-ray source onto the Rowland circle (RC) having a diameter equal to the crystal radius of curvature. Rays of all energies are diffracted through a slit aperture and are dispersed onto the RC. If the spectrometer is optimized for large dispersion and minimal instrumental broadening, then a detector

placed on the RC is illuminated by well-resolved and narrow spectral lines, narrower than the detector's intrinsic spatial resolution. In this case, the measured spectral line shape primarily results from the detector's LSF with small instrumental contribution.

The x-ray spectra were produced by the Naval Research Laboratory's Gamble II megavolt pulsed power generator with nominal operating output discharge of 2 MV peak voltage, 700 kA peak current, and 70 ns duration [3]. As shown in Fig. 1, rays from the source passed through a thick front aperture plate onto the crystal. The rays were diffracted by the bent crystal through a slit machined from thick tungsten blocks and were dispersed onto the CCD detector placed on the RC. There is no direct line-of-sight path from the source to the detector, and this facilitated the placement of the tungsten shielding and the mitigation of scattered gamma rays. Thick shielding also protected the CCD from scattered rays. In general, the placement of shielding was optimized so that the CCD detector viewed the crystal through the slit, had minimal views of other spectrometer internal surfaces that could scatter rays to the detector, had no direct view of the source, and was shielded from rays scattered toward the detector's side and back directions [4,5].

The spectrometer produces two mirror-image spectra on either side of the spectrometer's central axis. The spectral coverage was limited by the aperture sizes and was typically 28 to 110 keV. Image plates were placed on the RC, adjacent to the CCD detector or on the opposite side of the spectrometer axis to record the same energy range recorded by the CCD, and the image plates were shielded from scattered rays similar to the CCD.

The CCD detector was a commercial dental x-ray sensor in a rugged, hermetically sealed package: Hamamatsu Inc. sensor model S8985-02 and drive electronics model C9266-02. The CCD had a 1.5 mm thick fiber-optic faceplate and a CsI fiber-optic scintillator designed for radiation hardness at 60 kV and 0.3 mSv (30 mR) dose. The CCD had 20 μm pixel size, 1700 by 1200 pixel format, and 100% fill factor. The sensor and drive electronics had a 600,000 electron full-well capacity, 60 electron readout noise, 250 electron/pixel/s dark current, and 12 bit analog-to-digital digitization.

Although the sensor had a built-in x-ray photodiode trigger, custom software was written to manually begin integration for a period of typically 20 s spanning the Gamble II shot, and a 16 bit file was automatically downloaded to the control computer at the end of the integration period. A dark image (without x-ray exposure) was subtracted from the x-ray image.

As shown in Fig. 1, the CCD and drive electronics were isolated from the electromagnetic pulse produced by the Gamble II machine by a fiber-optic data cable. The control computer was located in a screen

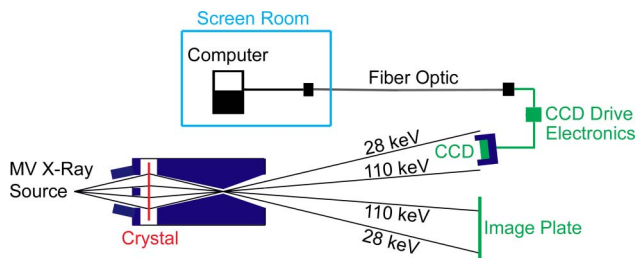


Fig. 1. (Color online) Schematic of the experimental setup of the spectrometer and the detectors (not to scale).

Table 1. Tungsten Characteristic K Transitions, Line Widths, and Relative Intensities

Transition	Energy (keV)	Observed Width		LSF Width		Relative Intensity			
		(eV)	(μm)	(eV)	(μm)	Theory	Observed		
$K\alpha_3$	KL1	$1s_{1/2} - 2s_{1/2}$	57.420	-	-	-	0.04	-	
$K\alpha_2$	KL2	$1s_{1/2} - 2p_{1/2}$	57.982	122	158	72	92	58.3	57.4
$K\alpha_1$	KL3	$1s_{1/2} - 2p_{3/2}$	59.319	124	154	74	93	100	100
$K\beta_3$	KM2	$1s_{1/2} - 3p_{1/2}$	66.952	171	166	121	117	11.4	10.7
$K\beta_1$	KM3	$1s_{1/2} - 3p_{3/2}$	67.245	152	146	101	98	21.9	18.6
$K\beta_5^{\text{II}}$	KM4	$1s_{1/2} - 3d_{3/2}$	67.652	-	-	-	-	0.18	-
$K\beta_5^{\text{I}}$	KM5	$1s_{1/2} - 3d_{5/2}$	67.716	-	-	-	-	0.32	-
$K\beta_2^{\text{II}}$	KN2	$1s_{1/2} - 4p_{1/2}$	69.032	169	154	101	108	2.8	1.9
$K\beta_2^{\text{I}}$	KN3	$1s_{1/2} - 4p_{3/2}$	69.101	150	137	100	91	4.8	3.6
$K\beta_4^{\text{II}}$	KN4	$1s_{1/2} - 4d_{3/2}$	69.267	-	-	-	-	0.05	-
$K\beta_4^{\text{I}}$	KN5	$1s_{1/2} - 4d_{5/2}$	69.283	-	-	-	-	0.08	-
KO	KO2,3	$1s_{1/2} - 5p_{1/2,3/2}$	69.484	-	-	-	-	1.1	-

room, and the fiber-optic cable spanned the distance to the CCD drive electronics box.

The fiber-optic link was SiTech Inc. model 2170 and was able to drive a cable up to 30 m in length. The fiber-optic drivers were connected to the computer and the CCD drive electronics by short USB cables. By optimizing the radiation shielding of the CCD and drive electronics, and communicating with the control computer in a distant screen room, a CCD x-ray image was captured on each TW-level discharge of the Gamble II generator without noticeable electromagnetic interference.

3. Tungsten Spectral Image

Using a geometrical model of the transmission crystal spectrometer [6], the spectrometer was designed to have high dispersion and small instrumental broadening. High dispersion was achieved by using a crystal with relatively small lattice spacing, quartz (203) with $2d = 0.275$ nm, and a large bending radius (and RC diameter) of 965 mm.

For the small Bragg angles used by the Cauchois spectrometer, the energy scale varied as the inverse of the distance from the spectrometer axis. For the detector positioned on the RC, the dispersion at the energy of the strongest W characteristic K transition, the $K\alpha_1$ transition at 59.319 keV listed in Table 1, was 16.2 eV per 20 μm CCD pixel. The natural width of this transition is 38 eV [7,8]. The 200 μm crystal thickness contributed an additional 15 μm instrumental broadening, while other instrumental broadening contributions, such as from the crystal rocking curve and geometrical aberrations were a factor of 10 smaller, and source broadening was similarly negligible when placing the detector on the RC [6]. Thus, the spectral line widths appearing in the CCD image primarily result from the LSF of the detector with contributions from the natural line width (46 μm , 2.3 pixel, 38 eV) and the crystal thickness (15 μm , 0.75 pixel, 12 eV).

Listed in Table 1 are the W characteristic K transitions, from the $n = 2$ levels (designated L) and higher levels (N, M, O) to the 1 s ground state in the singly ionized atom, and the transition energies [9].

The relative intensities are also listed with the strongest $K\alpha_1$ transition normalized to 100 [10]. Shown in Fig. 2 is a simulated spectrum calculated by convolving each transition with a Lorentzian profile having a full width at half-maximum (FWHM) value of 50 eV, which is the sum of the natural width (38 eV) of the $K\alpha_1$ transition and the instrumental broadening resulting from crystal thickness (12 eV). The vertical lines are the transition energies. Figure 2 illustrates the relative intensities and blending of the spectral features expected to be recorded by a CCD detector having single pixel resolution. The spectral resolution achieved in practice is less than ideal because of spreading in the scintillator; in addition, the weakest transitions were not observed because of the background of scattered high-energy rays from the Gamble II discharge and the limited dynamic range of the CCD.

An 800 by 800 pixel region of a single-shot spectral image is shown in Fig. 3(a). The dispersion is horizontal with energy increasing from left to right, and the W transitions appear as vertical lines. A random background is present in the dispersed spectral image, which is not correlated with the spectral lines. The background is much lower in a region of the CCD image (not shown) that was directly behind

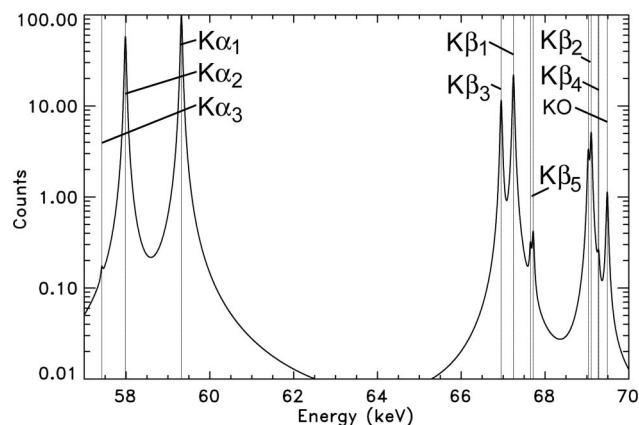


Fig. 2. Simulated x-ray spectrum calculated by convolving Lorentzian profiles having 50 eV FWHM with the transitions listed in Table 1. The vertical lines are the transition energies.

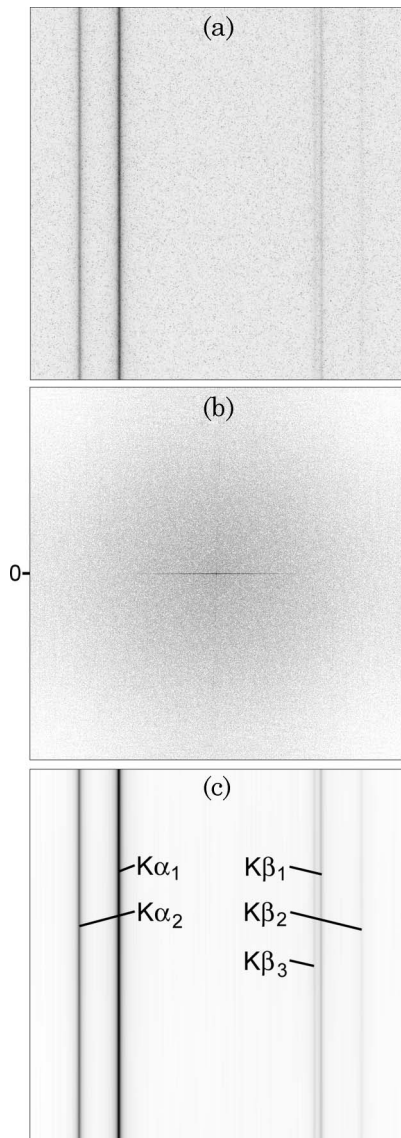


Fig. 3. (a) Spectral image recorded by the CCD detector from a single discharge of the Gamble II x-ray generator, where the coordinates are x and y . (b) Fourier transform of the x-ray spectral image, where the coordinates are spatial frequency k_x and k_y . The central horizontal row ($k_y = 0$) is indicated and contains the spectral lines, which are practically homogeneous in the vertical direction of the spectral image. (c) Spectral image with the background removed by Fourier analysis, where the coordinates are x and y as in (a).

the detector's x-ray shielding. This background, outside the region of the CCD image containing the dispersed spectral image, decreased with improved shielding that was developed during the experimental run but could not be completely eliminated from the spectral image. The background is attributed to harder x-rays scattered from the spectrometer's internal surfaces and will be the subject of future research.

4. Fourier Analysis

The two-dimensional Fourier transform (FT) of the spectral image is shown in Fig. 3(b), where the coordinates are spatial frequency k_x and k_y . The FT

was calculated using a fast Fourier transform algorithm of the type described in [11].

Because the spectral lines are practically homogeneous in the vertical direction in the spectral image, the central horizontal row of the FT image at $k_y = 0$ [indicated in Fig. 3(b)] is the FT of the spectral lines, while the remainder of the FT image contains the random background. It is, therefore, possible to remove the background by retaining only the central $k_y = 0$ row of the FT. The inverse FT of the central row is shown by the curve in Fig. 4. For comparison, the dots in Fig. 4 are the central row of the spectral image shown in Fig. 3(a) having no background removal, and the spectral lines are marginally visible above the background level. Retaining only the central row of the FT image, the absolute value of the inverse FT of the entire image is shown in Fig. 3(c), and the visibility of the spectral lines is greatly improved when the background is removed. We note that faint vertical features are present in Fig. 3(c) at the few-count level, which are retained along with the bright vertical spectral lines. Pixel count analysis of the CCD image of Fig. 3(a) indicates similar faint features are present in the unprocessed CCD image and probably represent a readout pattern. In any case, these features do not significantly affect the spectral image.

The small residual high-frequency noise in the curve shown in Fig. 4 is further reduced by summing the spectral image of Fig. 3(c) in the vertical direction. The resulting spectrum is shown by the data points in Figs. 5(a) and 5(b), covering the $K\alpha$ and $K\beta$ transitions, respectively. The high-frequency noise in the curve of Fig. 4, in the dispersion direction and perpendicular to the spectral lines, is believed to be primarily numerical noise caused by the discrete sampling of the spectral image by the CCD. The noise is different for each row of the spectral image of Fig. 3(c), and this results in smoothing when the rows are summed.

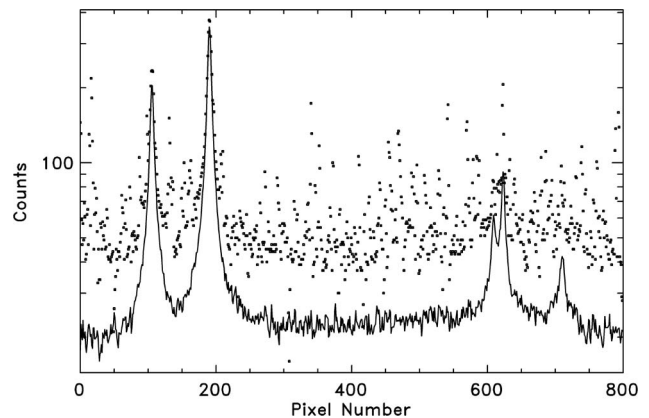


Fig. 4. Curve is the single row from the spectral image with the background removed by Fourier analysis. The dots are a single row from the spectral image recorded by the CCD and without background removal.

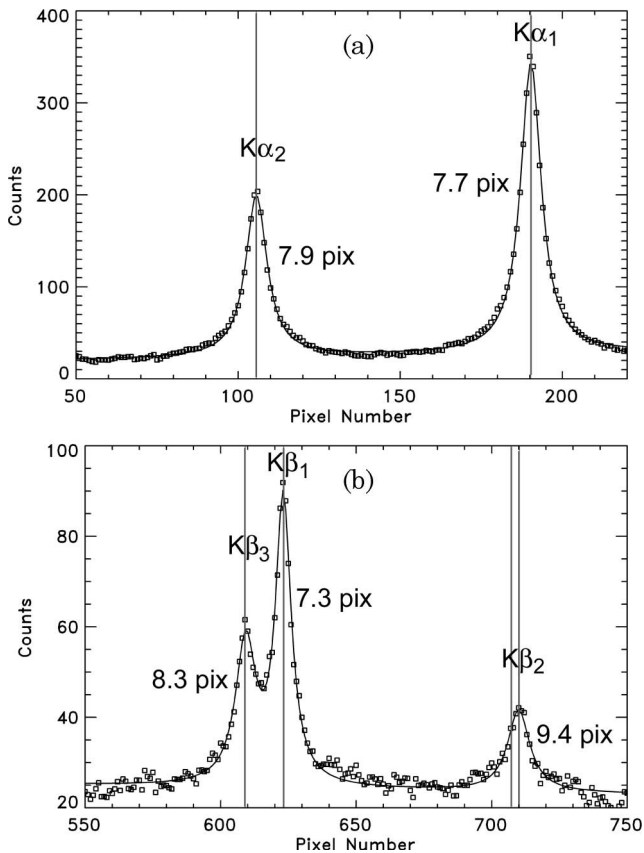


Fig. 5. Data points are the experimental spectra with background removed, and the curves are (a) two Lorentzians fitted to the $K\alpha_1$ and $K\alpha_2$ lines and (b) three Lorentzians fitted to the $K\beta_3$, $K\beta_1$, and $K\beta_2$ lines. The FWHM pixel values of the Lorentzians are indicated, and the vertical lines are the theoretical energies.

The curves in Fig. 5 are fits of Lorentzian profiles to the spectrum data points by the least-squares technique. Two Lorentzians were fitted to the $K\alpha$ features and three were fitted to the $K\beta$ blended features, and the FWHM values are indicated in Fig. 5. It is seen that the spectral features have FWHM pixel widths in the 7.3 to 8.3 range, with the exception of the $K\beta_2$ feature, which has a significantly larger 9.4 pixel width. This is because the $K\beta_2$ feature in Fig. 5(b) is an unresolved blend of two transitions from the $4p_{1/2}$ and $4p_{3/2}$ upper levels as listed in Table 1 and indicated in Fig. 2.

A Lorentzian curve fits each of the isolated (unblended) spectral lines very well, and this enables the removal of at least a portion of the Lorentzian width from the experimentally observed spectrum by Fourier analysis. The FT of a Lorentzian is an exponential. The FT of the strongest spectral line, the $K\alpha_1$ line, is shown by the data points in Fig. 6, and the solid curves are exponential fits to the low-frequency data points, appearing as straight lines on the logarithmic plot. These exponential curves intersect the high-frequency data points at a frequency of approximately 14/pixel, consistent with the 7.7 pixel FWHM of the Lorentzian fitted to the $K\alpha_1$ line.

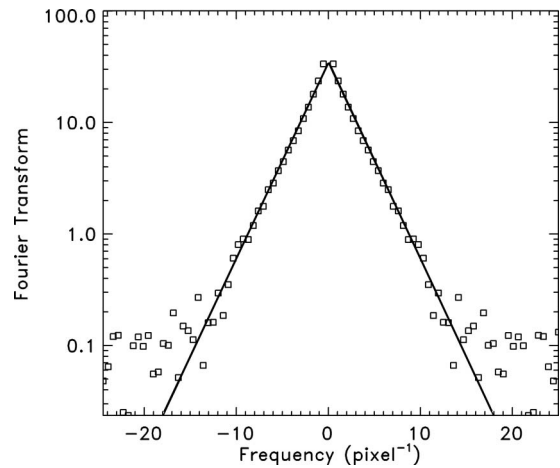


Fig. 6. Data points are the Fourier transform of the $K\alpha_1$ line, and the two curves are fits to the low-frequency data points and represent the exponential FT of a Lorentzian.

The Lorentzian width is removed from the experimental spectrum by dividing the FT of the spectrum by the FT of the Lorentzian and taking the inverse FT. This technique is effective when the background level is low, as for the two $K\alpha$ lines in Fig. 5(a), but is not so effective for the weaker $K\beta$ lines with

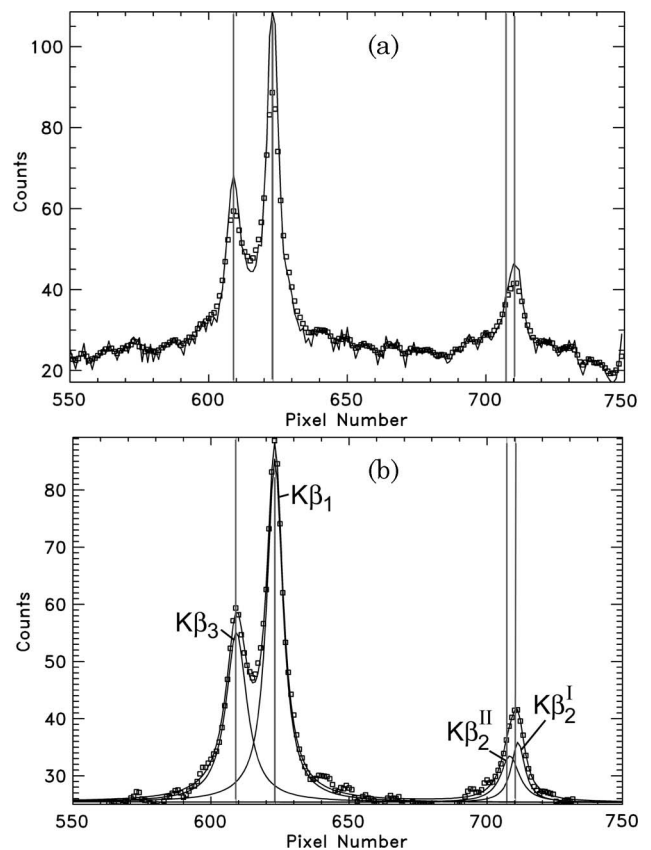


Fig. 7. Data points are the experimental spectrum covering the $K\beta_3$, $K\beta_1$, and $K\beta_2$ features with background removed. (a) Curve is the spectrum after removal of half the width of the Lorentzian LSF by Fourier analysis. (b) Curves are the fits of four Lorentzians to the spectrum. The vertical lines are the theoretical energies.

lower signal-to-background level. This is illustrated in Fig. 7(a), where half of the (low-frequency) Lorentzian width was removed from the $K\beta$ lines, but the high-frequency background level is not suppressed. While high-frequency background suppression techniques can be implemented, the algorithms are complicated and can introduce artifacts into the derived spectrum. A simpler and more effective technique is to fit multiple Lorentzians to the blended spectral features. This is illustrated in Fig. 7(b), where the $K\beta_2$ feature is fitted by two Lorentzians representing the $K\beta_2^I$ and $K\beta_2^{II}$ transitions listed in Table 1.

The final FWHM values of the Lorentzians fitted to the observed $K\alpha$ and $K\beta$ features are listed in Table 1. The CCD detector's intrinsic LSF is determined by removing the natural and instrumental widths from the spectral line widths recorded by the detector. The natural line profiles are Lorentzian in shape and have known widths [7,8]. The convolution of two Lorentzians with FWHM values w_1 and w_2 is a Lorentzian with FWHM value $w_1 + w_2$. Thus, the Lorentzian natural widths are easily removed by subtraction from the recorded Lorentzian widths. While the shape of the instrumental profile resulting from crystal thickness is not known, this width is small ($15\ \mu\text{m}$) and can be removed by subtraction without significant error. As seen in Table 1, the LSF FWHM values, in units of micrometers, do not change substantially with energy in the 58 to 70 keV range that was studied. The LSF FWHM values, in units of eV, of the $K\beta$ lines are somewhat larger than for the $K\alpha$ lines because of the decreasing spectrometer dispersion with energy.

The relative intensities, the areas under the observed Lorentzian curves, are listed in Table 1, where the $K\alpha_1$ intensity is normalized to 100. The measured relative intensities are in agreement with the theoretical values except that the measured/theoretical intensity ratios of the $K\beta$ lines decrease with energy. Some of the decrease is attributable to the decreasing crystal efficiency and CCD detector sensitivity with increasing energy.

The average LSF FWHM value, in units of micrometers, was calculated by weighting the FWHM values of the six observed spectral lines by their relative intensities, as listed in Table 1. The weighted average value is $95\ \mu\text{m}$ with $6\ \mu\text{m}$ standard deviation (4.75 ± 0.3 pixel).

5. Discussion

The detailed Fourier analysis of the spectral image recorded by an x-ray CCD detector indicates the detector's line spread function (LSF) is Lorentzian in shape with an average FWHM value of $95\ \mu\text{m} \pm 6\ \mu\text{m}$ (4.75 ± 0.3 pixel) in the 58 to 70 keV energy range. This value was determined by removing the natural line width and the instrumental broadening caused by crystal thickness from the experimentally measured spectral line widths. Source size broadening of the spectral lines is negligible because the

detector was placed on the Rowland circle where monoenergetic rays from an extended source are focused. In addition, source energy broadenings caused by the Doppler or Stark effects are negligible in the hard x-ray region. While other instrumental broadenings, such as spectrometer aberrations and the crystal rocking curve contribution, are believed to be negligible [6], if present they would tend to reduce the inferred detector LSF below the $95\ \mu\text{m}$ value.

The LSF of two types of image plates, Fuji SR and MS, were found to be Gaussian with $130\ \mu\text{m}$ FWHM and Lorentzian with $190\ \mu\text{m}$ FWHM, respectively [1]. This implies the CCD detector has superior LSF. However, the larger dynamic range and typically higher signal-to-background level in the image plate scan files can enable accurate determination of the LSF, which can be removed from the image plate spectral data as done for the CCD data. The choice of image plate or CCD detection in hard x-ray spectroscopy and radiography depends on the experimental conditions, nature and quality of the spectral data, and the desired science result.

We note that the energy positions and relative intensities of the features observed in the tungsten spectrum from the Gamble II generator are essentially the same as for the characteristic x-ray transitions in singly ionized W atoms listed in Table 1, with the caveat that the measured/theoretical $K\beta$ intensity ratios decrease with energy because of the decreasing crystal and detector efficiencies. The observed symmetrical Lorentzian line shapes are further evidence that the features are transitions from cold W atoms and not shifted to higher energy by ionization. The estimated energy shift of the K shell transitions with ionization of outer electrons is approximately 1 to 2 eV per ionized electron. Assuming energy shifts of 0.1 in the FWHM values would produce noticeable asymmetries in the line profiles, we conclude that the ionization of outer electrons is less than 10, at least during the time of strongest line emission, which dominates the time-integrated CCD spectral image. This is consistent with computational modeling of the Gamble II plasma conditions, which indicates that the temperature is 25 eV and the average ionization is $\langle Z \rangle \approx 12$ at the time of peak energy density, and later in the discharge a peak temperature of 60 eV and $\langle Z \rangle \approx 20$ occur.

The mention of commercial products does not imply endorsement by the U. S. government or that the mentioned commercial products are the best for the application. This work was supported by the Defense Threat Reduction Agency (C-WMD Basic Research Program) and by the Office of Naval Research (ONR).

References

1. J. F. Seely, G. E. Holland, L. T. Hudson, and A. Henins, "Modulation transfer functions of photo-stimulable phosphor image plates and scanners," *Appl. Opt.* **47**, 5753–5761 (2008).

2. L. T. Hudson, R. D. Deslattes, A. Henins, C. T. Chandler, E. G. Kessler, and J. E. Schweppe, "A curved crystal spectrometer for energy calibration and spectral characterization of mammographic x-ray sources," *Med. Phys.* **23**, 1659–1670 (1996).
3. B. V. Weber, R. J. Commisso, G. Cooperstein, D. D. Hinshelwood, D. Mosher, P. F. Ottinger, D. M. Ponce, J. W. Schumer, S. J. Stephanakis, S. B. Strasburg, S. B. Swanekamp, and F. C. Young, "Ultra-high electron beam power and energy densities using a plasma-filled rod-pinch diode," *Phys. Plasmas* **11**, 2916–2927 (2004).
4. N. R. Pereira, B. V. Weber, J. P. Apruzese, D. Mosher, J. W. Schumer, J. F. Seely, C. I. Szabo, C. N. Boyer, S. J. Stephanakis, and L. T. Hudson, "K-line spectra of warm, dense plasmas produced with intense pulsed electron beams," *Rev. Sci. Instr.* (to be published). A preprint is available online at http://spectroscopy.nrl.navy.mil/spectroscopy_website_003.htm.
5. M. S. Litz, G. Merkel, N. R. Pereira, C. N. Boyer, G. E. Holland, J. W. Schumer, J. F. Seely, L. T. Hudson, and J. J. Carroll, "Anomalous fluorescence line intensity in megavoltage bremsstrahlung," *Phys. Plasmas* **17**, 043302 (2010).
6. J. F. Seely, L. T. Hudson, G. E. Holland, and A. Henins, "Enhanced x-ray resolving power achieved behind the focal circle of Cauchois spectrometers," *Appl. Opt.* **47**, 2767–2778 (2008).
7. J. B. Krause, "Atomic radiative and radiationless yields for K and L shells," *J. Phys. Chem. Ref. Data* **8**, 307–327 (1979).
8. J. Scofield, "Exchange corrections of K x-ray emission rates," *Phys. Rev. A* **9**, 1041–1049 (1974).
9. R. Deslattes, E. Kessler, P. Indelicato, and E. Lindroth, "X-ray wavelengths," in *International Tables for Crystallography, Vol. C. International Union of Crystallography*, A. J. C. Wilson and E. Prince, eds. (Kluwer Academic, 1999), p. 206.
10. G. P. Williams, "X-ray properties of the elements," Section 1 in *X-Ray Data Booklet*, xdb.lbl.gov.
11. W. H. Press, B. P. Flannery, S. A. Teukolsky, and W. T. Vetterling, *Numerical Recipes* (Cambridge U. Press, 1989).